Simulation of flow and transport processes in a discrete fracture-matrix system I. geostatistical generation of fractures on an aquifer analogue scale

A. Assteerawatt H. Hægland R. Helmig A. Bárdossy
H. K. Dahle

Abstract

Aquifer-analogue studies established in the petroleum industry have been widely used for characterizing fractured aquifer systems. Detailed analysis can be performed practically on an analogue scale and characteristics of fractured systems obtained on this scale can be upscaled to field scales. A discrete fracture-matrix model is an attractive alternative for studying on the analogue scale compared with single- and multi-continuum models since the effect of individual fractures can be explicitly investigated. The critical step for the discrete fracture model is the generation of a "representative" fracture network. In general, fracture networks are generated by describing fracture geometries in terms of statistical distribution and often neglecting the spatial variability. This tool is a so-called statistical fracture generator. In this study, we develop a geostatistical fracture generator which integrates statistical geometries and spatial characteristics in terms of a standardized variogram, neighborhoods and a fracture-cell density. Later the flow and transport behavior of a fracture-matrix system is investigated. We show that fracture networks generated by the GFG, to some extent, represent not only the included spatial characteristics but also a desired fracture-distance distribution (which is not considered in the GFG itself), and can better capture the flow and transport behavior of the fracture-matrix system (discharge, peak arrival time, and mean arrival time) than the fracture networks generated by the SFG. Hence, integrating the spatial characteristics and the statistical geometries in the GFG have improved the discrete fracture generation and the flow and transport behavior of the fractured system can be better predicted.

1 Introduction

For many countries worldwide, fractured rock systems have provided important natural resources such as petroleum, gas, water and geothermal energy. Many recent studies investigate the suitability of fractured systems as storage/disposal sites for high-level nuclear waste ([10, 11, 30, 12]). The resource exploitation and potential utilization have led to extensive studies with the aim of understanding, characterizing and finally predicting the behavior of fractured rock systems. Aquifer-analogue studies have been widely used for characterizing fractured systems ([2]). In the analogue studies, the detailed analysis of fractured systems such as borehole samplings, hydraulic measurements or exposed wall investigations can be performed practically, and the flow and transport properties obtained on the analogue scale can be upscaled to the field scale ([18]). On the large reservoir scale, the fractured system is considered as a single- or double-continuum, however, on the analogue scale, this assumption is not always valid. Long et al. [25] showed that the validity of considering a fractured system

as a continuum depended on the geometries of the fractured system, e.g. density and orientation. For the aquifer analogue studies, a discrete fracture model is an attractive alternative compared with a continuum model because there is no a priori assumption that the fractured system behaves as a continuum, and the effect of individual fractures can be explicitly investigated. The increased speed of computers nowadays makes even computationally demanding simulations, which is the main drawback of the discrete approach, feasible on the analogue scale. The critical step for the discrete model approach is the generation of a "representative" fracture network ([28]). In general, fracture network generators can be categorized as: a) deterministic fracture generators (DFG), and b) statistical fracture generators (SFG). The geometries of a fracture network (e.g. size, aperture, orientation and location) are determined exactly for the individual fractures in DFG, whereas they are represented by statistical distribution functions in SFG ([23, 19, 36, 13]). Due to the intensive data requirements in DFG, SFG is generally more practical. In the case where dominating fractures are known, a combination of SFG with DFG is required. However, SFG often fails to capture spatial variability and connectivity of fracture networks, which is related to interconnected flow paths that may dominate flow and transport processes in fractured systems ([8]). Spatial variability of fracture networks has been observed in many studies. La Pointe and Hudson [22] showed that fracture density and fracture orientation can follow a systematic spatial pattern. For a large scale problem, the attempt to incorporate spatial variability was presented by Long and Billaux [24]. They evaluated the experimental variogram of fracture traces from a drift wall and generated a two-dimensional heterogeneous fracture network which contained statistically homogeneous sub-domains. This concept was extended to generate a three-dimensional fracture network of circular-disc fractures by Billaux et al. [9]. However, on the analogue scale, assuming fracture geometries to be variable in the whole domain and homogeneous in sub-domains is not applicable because the domain size relative to the fracture size is relatively small.

The objective of this study is to develop a geostatistical fracture generator (GFG) which directly handles the statistical geometries as well as the spatial variability. We characterize spatial variability and connectivity of a fracture network from exposed walls (outcrops, tunnels or drifts) and consider these parameters in the geostatistical fracture generator (GFG). To our knowledge this is the first time that spatial connectivity of fractures is directly included in fracture generators. In the GFG, first a fracture network is generated by the statistical fracture generator (SFG) developed by Silberhorn-Hemminger [32] and then its spatial characteristics are included using a global optimization method known as Simulated Annealing (SA). A successful application of SA in optimizing spatial problems concerning fractured systems have been reported by several authors ([17, 4, 16, 34]). The flow and transport behavior of a fractured system are investigated to compare the fracture network generated by the GFG and the SFG. In this study, the fractured system describes a fracture network embedded in a surrounding matrix which is permeable to flow, although less permeable than the fractures by several orders of magnitude. This type of a fractured system is commonly called a fractured porous media or a fracture-matrix system (FMS).

The paper is organized as follows. In Section 2, we introduce the methodology to quantify spatial characteristics from exposed walls. In Section 3, the GFG based on the statistical geometries and the analyzed spatial variability is presented. A comparative study of fractured systems where fracture networks are generated by the GFG and by the SFG is performed in Section 4. In Section 5, we summerize the results and discuss future research work.

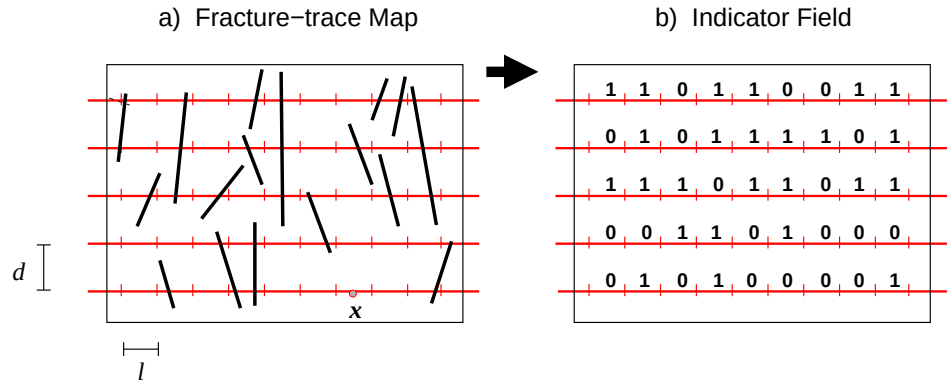

Figure 1: Procedure of evaluating an indicator field from a fracture-trace map.

2 Analysis of Spatial Characteristics

We quantify the spatial characteristics of the fracture network from fracture-trace maps of exposed walls by the *modified scanline technique* (MS) ([18]). In Figure 1, the scanline method is illustrated. First, a set of parallel and equally-distributed scanlines are overlayed on a fracture-trace map, where the direction of scanlines is arranged perpendicular to the main orientation of the fracture traces. The scanlines are divided into segments of equal length l. The fracture trace map is hence divided into a grid of cells, see Figure 1b. Then, along each scanline, the existence of intersection points between fracture traces and the scanline segment itself are recorded and described with an indicator variable $I(\boldsymbol{x})$:

$$I(\boldsymbol{x}) = \begin{cases} 1 & \text{intersection fracture-scanline exists (called fracture cell)} \\ 0 & \text{no intersection fracture-scanline exists (called matrix cell)} \end{cases} . \tag{1}$$

Here $\boldsymbol{x}$ is a discrete variable that represents the midpoint of a cell. In this way, the fracture trace map is transformed into an indicator field. The distance d between scanlines, and the length l of the scanline segment, are defined depending on the size of the fracture-trace maps and the characteristics of the fracture traces. Different scanline distances and scanline segments should be investigated in order to find suitable values ([18]).
The study site in this work is a field block of $8 \times 10 \times 2$ m located at Pliezhausen, Germany (see Figure 2). The field block is characterized by dense fractures and high porosity and permeability of the matrix. The fracture trace maps are recorded from a surface of five exposed walls by performing stereophotogrametric shooting ([18]). Figure 3 shows the fracture traces recorded on the five exposed walls: the north, the east, the south-east, the south-west and the west walls. Three main fracture clusters, one with almost horizontal orientation and two with almost vertical orientations, are identified from the 3D field block using stereographic projection, however only two main directions of fracture traces are observed on the 2D exposed walls: one horizontal, and one vertical. Since the scanline direction has to be perpendicular to the main direction of the fracture trace, two scanline directions are required. Two indicator fields are evaluated from each exposed wall: one for the horizontal scanline direction considering vertical fracture traces and another one for the vertical scanline direction considering horizontal fracture traces. According to the analysis of the Pliezhausen exposed walls presented in Silberhorn-Hemminger [32], the experimental variogram evaluated from the scanline distance $d = 0.10$ m (for the horizontal scanline) and $d = 0.20$ m (for the vertical

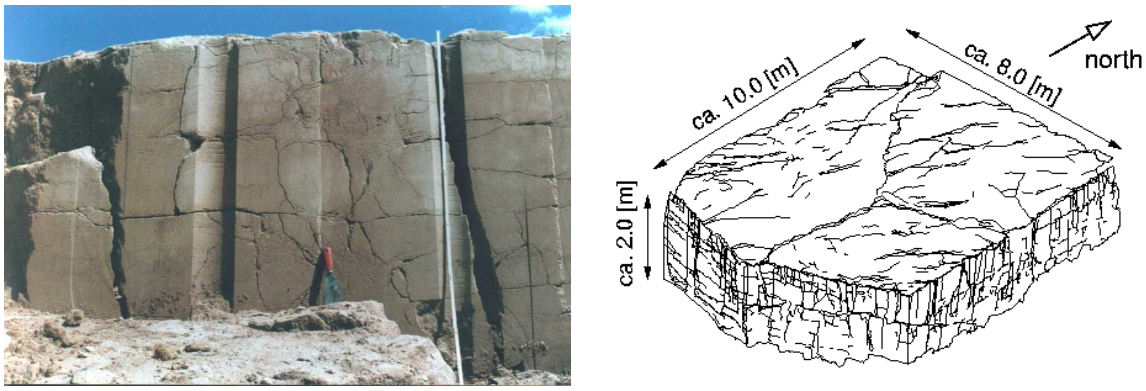

Figure 2: The field block and scanned view of the field block from the south-east (modified from Dietrich et al. [18]).

scanline) showed similar characteristic for either segment length of 0.04 or 0.10 m. Therefore, the segment length $l = 0.10$ m is selected in this study because it economizes computation time for our further spatial analysis.
The spatial variability is analyzed from indicator fields considering the vertical and the horizontal fracture trace. The first parameter is a standardized experimental variogram, which measures the average of an increment of values between two points, and at the same time, considers the variability of the indicator fields in terms of the variance σ^2:

$$\gamma_s(\boldsymbol{h}) \;=\; \frac{1}{2\sigma^2}\;\left(\frac{1}{n_h}\sum_{\alpha=1}^{n_h}\left[I(\boldsymbol{x}_\alpha+\boldsymbol{h})\;-\;I(\boldsymbol{x}_\alpha)\right]^2\right)\;, \tag{2}$$

where the separation vector $|\boldsymbol{h}|$ is measured parallel to the main direction of the fracture trace (perpendicular to the scanline direction) and n_h is the total number of pairs of variables at a distance $|\boldsymbol{h}|$ apart. Since the indicator variables can have two possible outcomes 0 and 1, its variance is then described according to a Bernoulli trial, which relates to a trial that can have two possible outcomes. The variance of the indicator field is then given by

$$\sigma^2 \;=\; p(1-p)\;, \qquad \text{where} \qquad p \;=\; \frac{1}{n}\sum_{\alpha=1}^{n} I(\boldsymbol{x}_\alpha)\;, \tag{3}$$

where p is the probability of being a fracture cell and n is the total number of cells.
Figure 4 shows that the standardized variograms of the five exposed walls increase within a specific distance $\boldsymbol{h}$, known as the correlation length or the range, and later reach a constant value, known as the sill. This means that a spatial dependency of the fracture trace exists within that range. Only the separation vector $\boldsymbol{h}$ parallel to the main direction of the fracture trace is considered in this paper; for $\boldsymbol{h}$ perpendicular to the fracture-trace direction, the experimental variograms of all exposed walls show only the nugget effect which means no spatial dependency, see Assteerawatt [3]. The average of the standardized experimental variograms of the five exposed walls are fitted with variogram models by VARIOWIN ([29]). The average experimental variograms show best fit with a combination of the exponential and the nugget variogram model ([14]):

$$\gamma(\boldsymbol{h}) \;=\; C_0 + C_1\,(1\;-\;e^{\left(-\frac{|\boldsymbol{h}|}{a}\right)}) \qquad \text{for} \quad a\;>\;0\;. \tag{4}$$

a) North exposed wall

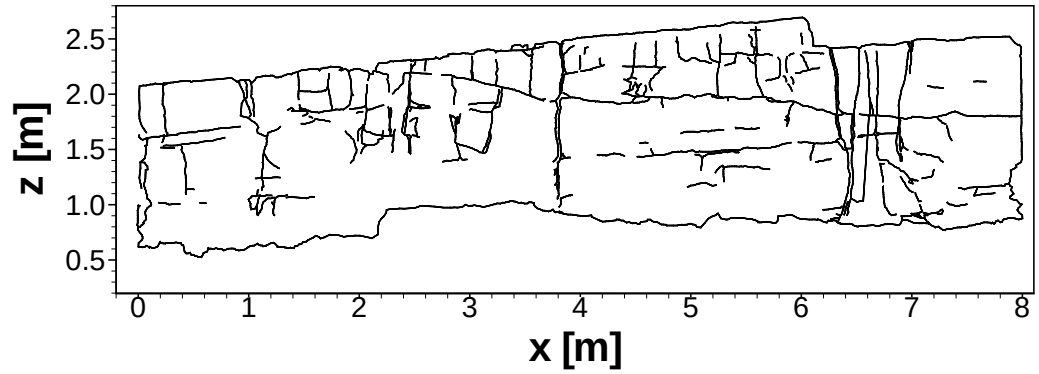

b) East exposed wall

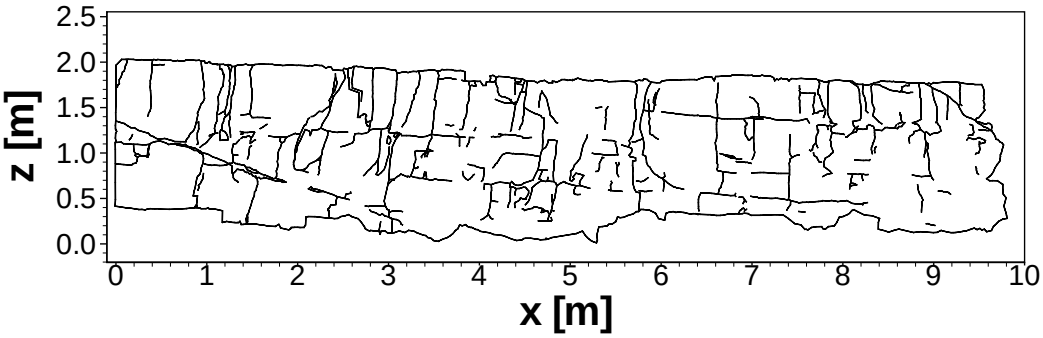

c) South-east exposed wall

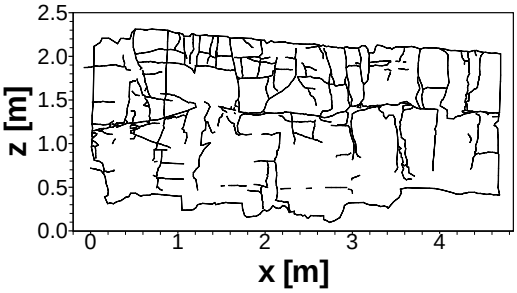

d) South-west exposed wall

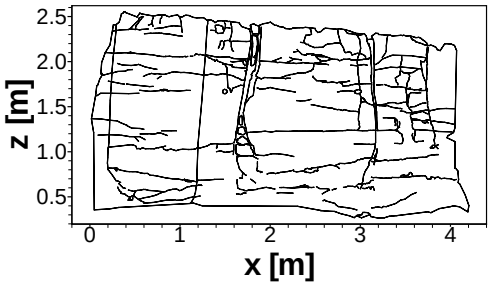

e) West exposed wall

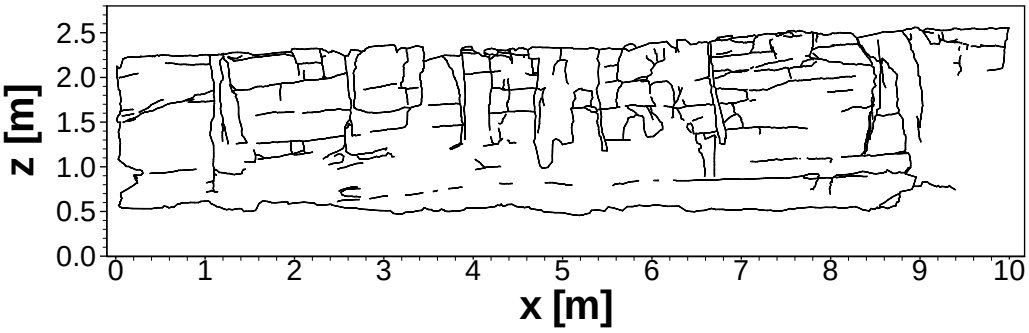

Figure 3: Fracture trace maps of the five exposed walls obtained from a Pliezhausen field block (modified from Dietrich et al. [18]).

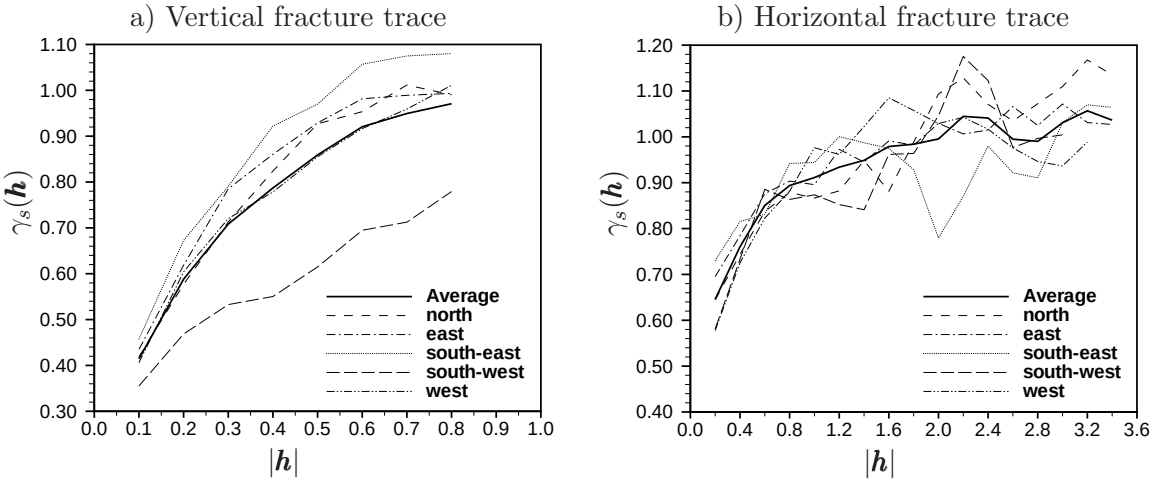

Figure 4: Standardized experimental variograms of the five exposed walls.

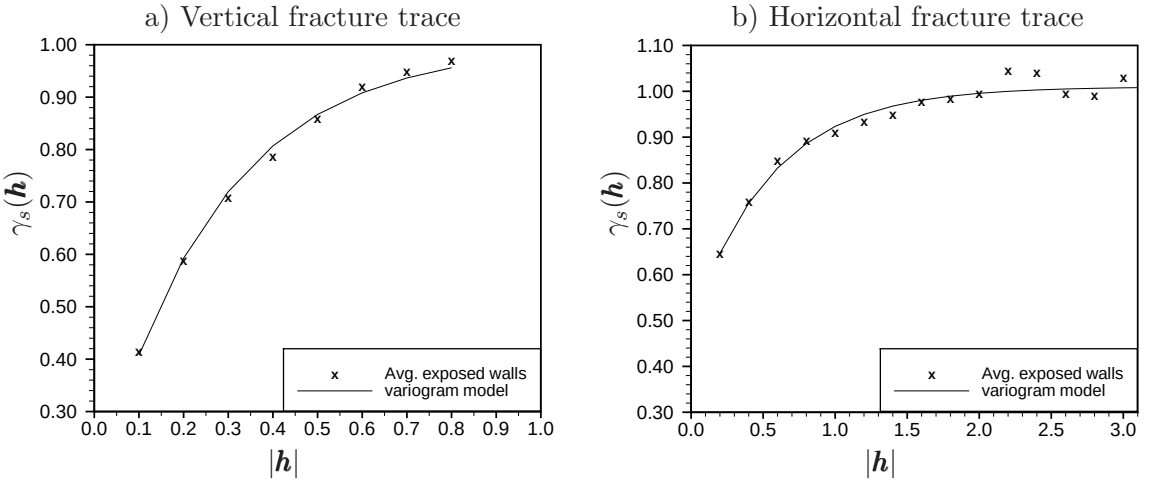

Figure 5: Variogram models from the average of the standardized experimental variograms.

The parameters C_0, C_1 and a, are 0.14, 0.86 and 0.80, respectively, for the horizontal-scanline indicator fields and 0.48, 0.52 and 1.67, respectively, for the vertical-scanline indicator fields. In this case, the sum of C_0 and C_1 is 1 because the experimental variograms are normalized by the variances. The best-fit variograms for the average values of all five standardized experimental variograms are shown in Figure 5. The standardized variogram only consider the spatial variability in the direction of the fracture trace, therefore, the additional parameters called neighborhoods are used to characterize the spatial connectivity of the fracture traces related to other directions. The fracture neighborhood N_f and the matrix neighborhood N_m describes the probability of finding a fracture cell or a matrix cell in the eight adjacent cells of a centered cell $I(\boldsymbol{x}_\alpha)$:

$$\begin{aligned} N_f(k) &= \tfrac{1}{n_f} \textstyle\sum_\alpha^n I(\boldsymbol{x}_\alpha^k) I(\boldsymbol{x}_\alpha) \ , \\ N_m(k) &= \tfrac{1}{n_f} \textstyle\sum_\alpha^n I(\boldsymbol{x}_\alpha^k)(1 - I(\boldsymbol{x}_\alpha)) \ . \end{aligned} \tag{5}$$

Here n is the total number of cells, n_f is the total number of fracture cells, $\boldsymbol{x}_\alpha^k$ is the adjacent cell located in direction k of $\boldsymbol{x}_\alpha$. The directions k, illustrated in Figure 6, are represented by the digits 0 to 7.

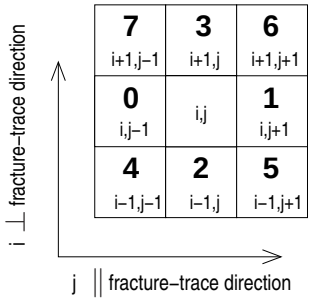

Figure 6: Illustration of neighborhood directions in connection with the digits 0 to 7.

The neighborhoods N_f and N_m of the five exposed walls from the vertical and the horizontal fracture trace are presented in Figure 7 and 8, respectively. Due to the values assigned in Equation (1), a high value of neighborhoods corresponds to a large number of fracture cells. A high value of N_f is clearly observed in the fracture-trace direction ($k = 2, 3$) as expected because neighboring cells of a fracture cell in the fracture direction have a tendency to be fracture cells. The N_m are significantly lower in the direction of fracture traces meaning that neighboring cells of a matrix cell in the fracture direction tend to be a matrix cell. The values of the neighborhoods in the other directions are related to the number of the fracture and the matrix cells found in those directions. If a center cell is a fracture cell and a neighboring cell in a non-fracture-trace direction ($k \neq 2, 3$) is also a fracture cell, this could indicate existence of a fracture trace in that direction, hence the spatial connectivity of fracture traces is related to the values of the neighborhoods.

Due to the weathering process acting on the exposed outcrop, the largest number of vertical fractures is observed on the top. For representing this fracture structure, we set up a parameter called fracture-cell density $H(z)$, where the z-coordinate increases towards the top of the outcrop. It is defined by the number of fracture cells relative to the total number of cells along each horizontal scanline. The fracture-cell density is only considered for the vertical fracture traces in the horizontal scanline direction. In Figure 9, the results from the five

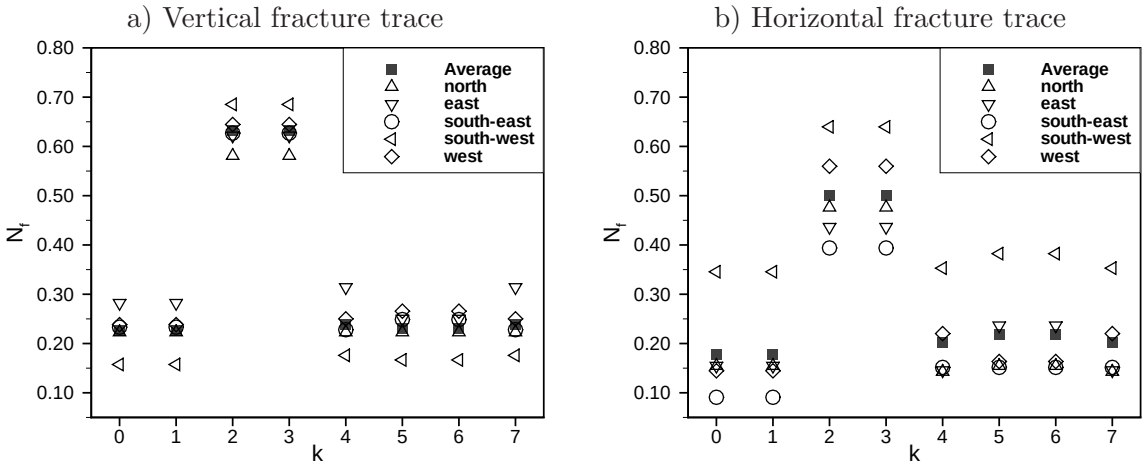

Figure 7: Fracture neighborhood of the five exposed walls.

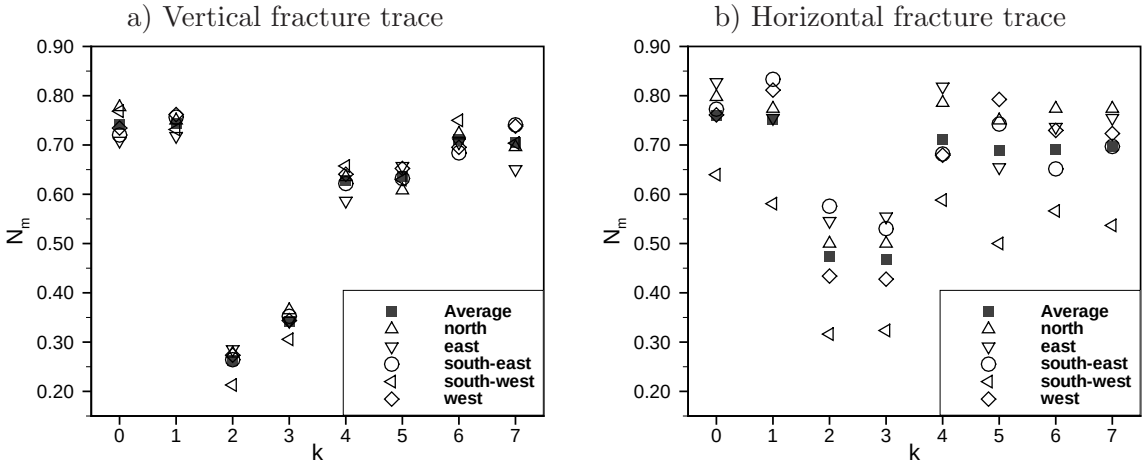

Figure 8: Matrix neighborhood of the five exposed walls.

exposed walls clearly show an increase of the number of fracture cells with increased vertical position z, which is in agreement with our observation.

The probability p expressed in Equation (3) is included as one of the parameters in the GFG in order to control the number of fracture cells and matrix cells. It is assumed to be constant and the average p evaluated from the horizontal- and vertical-scanline indicator fields are 0.2112 and 0.2377, respectively.

The spatial parameters which are analyzed from the outcrop block are considered as spatial characteristics of the outcrop fracture network. The geostatistical fracture generation (GFG) is carried out in the next section by integrating the spatial characteristics which are discussed in this section and the statistical geometries of the fracture network such as the fracture orientation, the fracture density and the fracture size.

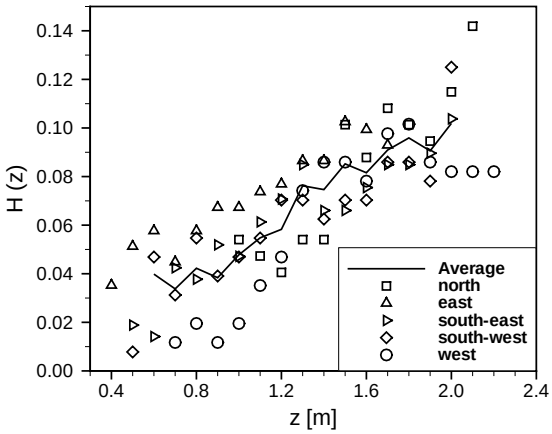

Figure 9: Fracture-cell density of the five walls for the vertical fracture traces.

3 Geostatistical Fracture Generation

The success of a simulated annealing (SA) as a global optimization method in integrating multiple characteristics of discrete fractures ([4, 35]), and its flexibility to incorporate additional information (if needed), make the SA attractive as a methodology for fracture-network generation. Additionally, the SA can locate good approximations to global optimum of a given objective function in a large search space ([1]). The application of SA in optimization problems concerning fractured systems have been reported by several authors ([26, 16, 34]). The objective function of the SA is defined as the difference between a set of reference properties from a desired configuration and from a candidate realization. The SA starts at an initial state, and the system is modified randomly to a new state. The new state is accepted if the change decreases the objective function or if the change increases the objective function, it is accepted with the probability

$$p_{acc} = \begin{cases} 1 & \text{if } O(S_2) \leq O(S_1) \\ e^{\left(-\frac{O(S_2)-O(S_1)}{T}\right)}, & \text{if } O(S_2) > O(S_1)\ . \end{cases} \tag{6}$$

Here the constant parameter T, called annealing temperature, is used for controlling the acceptance of the new state, and $O(S_1)$ and $O(S_2)$ are the values of the objective function of the current state (S_1) and the new state (S_2), respectively. At each temperature, the perturbation is repeated for a large number of iterations M before decreasing the temperature. The temperature T is then reduced linearly to a new temperature T_{new} with the cooling factor α, $T_{new} = \alpha\, T$. When the temperature T becomes lower, the probability of accepting changes which cause high objective functions, becomes smaller. This allows the problem to converge. The SA is used as a methodology in the GFG for integrating the desired spatial characteristics in the generated domain. The GFG was implemented in the existing 3D-fracture generator *FRAC3D* developed by Silberhorn-Hemminger [32]. The FRAC3D originally offers two different approaches: the deterministic fracture generator (DFG) and the statistical fracture generator (SFG). The DFG requires exact information of a fracture network and the SFG assumes that a fracture network can be described by theoretical distribution of its geometries such as orientation, size and density. The SFG starts with generating a random midpoint of a fracture and determines the location of the fracture from its orientation and size. The

newly generated fracture is included into the global list of fractures until the desired fracture density is reached. This approach is based on univariate statistics and does not include any information about the spatial variability. Optimizing the fracture distance, which is defined by distances between two directly adjacent fractures measured along a reference line, is an optional step in the SFG that can be used to include spatial information in the generation of a fracture network ([32]).

The GFG takes into account the statistical geometries and the spatial variability of the indicator fields (the standardized experimental variogram, the neighborhoods, the fracture-cell density and the variance), see Assteerawatt [3]. The GFG starts by generating an initial state of the fracture network using the SFG. Thus, the generated fracture network obeys the statistical geometries (size, orientation and density). By defining several investigated cross-sections in the generated domain, the spatial parameters can be evaluated from the investigated cross-sections. The objective function $O(k)$ of the randomly generated system is defined as the sum of normalized differences between the spatial parameters of the target fracture network ($\hat{\gamma_s}(\boldsymbol{h})$, $\hat{N}_f(j)$, $\hat{N}_m(j)$, $\hat{H}(z)$ and $\hat{\sigma}^2$) and of the generated fracture network at state k ($\gamma_s^k(\boldsymbol{h})$, $N_f^k(j)$, $N_m^k(j)$, $H^k(z)$ and ${\sigma^k}^2$) from all N_e investigated cross sections:

$$\begin{aligned} O(k) \;=\; & \sum_{i=1}^{N_e}\Big(w_1 \sum_{j=1}^{n_{\gamma_s}} \frac{|\hat{\gamma_s}(\boldsymbol{h}_j) - \gamma_s^k(\boldsymbol{h}_j)|}{\hat{\gamma_s}(\boldsymbol{h}_j)} \;+\; w_2 \sum_{j=0}^{7} \frac{|\hat{N}_f(j) - N_f^k(j)|}{\hat{N}_f(j)} \\ & + w_3 \sum_{j=0}^{7} \frac{|\hat{N}_m(j) - N_m^k(j)|}{\hat{N}_m(j)} \;+\; w_4 \sum_{j=1}^{n_H} \frac{|\hat{H}(z_j) - H^k(z_j)|)}{\hat{H}(z_j)} \\ & + w_5 \frac{|\hat{\sigma}^2 - {\sigma^k}^2|}{\hat{\sigma}^2}\Big)\,, \end{aligned} \tag{7}$$

where w_i is the weighting function and $\sum w_i = 1$. By introducing the weighting function, the influence of each spatial parameter on the objective function can be controlled. After evaluating the objective function of the current state from Equation (7), the fracture network is modified to a new configuration and a new objective function value is calculated. Comparing the two objective functions, the new network is accepted with the acceptance criteria mentioned in Equation (6). The fracture network is modified at each iteration step by adding/removing one fracture, or randomly selecting one fracture and changing its geometries (location, orientation or shape). All fractures are convex polygons consisting of four to seven edges. The fracture shape is modified by adding/removing a corner point under the constraint of a total number of the corner points, or by moving a corner point. The perturbation is carried out for M iterations and then the temperature T is reduced related to the cooling factor α. Finally, the SA stops when the objective function remains unimproved after a couple of temperature steps, or the minimum temperature T_{stop} is reached. The configuration with a minimum objective function is regarded as the solution to the problem of finding a realization which has spatial characteristics closest to the target fracture network. The major difficulty in applying SA is that there is no obvious analogy for defining the initial temperature T_0, the number of iterations M, and the cooling factor α at each temperature step. In accordance with Bárdossy [5], the value of the initial temperature T_0 is selected so that the initial acceptance probability of a new stage is approximately 0.80 for assuring that many "bad" configurations which do not improve the objective function are accepted in the beginning. The number of iterations M is defined as half of the total number of fractures, to ensure a high probability of the generated fractures to be involved in the exchange processes.

Typical values of the cooling factor α for moderately slow cooling rates are 0.90 through 0.99. In this work, the cooling factor of 0.90 is selected and remains constant for all temperature steps.

4 Comparison of Geostatistical and Statistical Fracture Generation

In this section, the fracture networks generated by the GFG and the SFG are compared. The distribution functions of fracture geometries observed on the Pliezhausen block are summarized in Table 1.

	Parameters of Distribution Function		
Orientation:			
Fisher Distribution	$f(\theta,\phi) = \frac{\kappa}{4\pi \sinh\kappa}\, e^{[\kappa\,(\sin\theta\,\sin\alpha\,\cos(\phi-\beta)+\cos\theta\,\cos\alpha)]\,\sin\theta}$		
	Azimuth (A)	Dip (D)	Spherical Aperture (ω)
	$A = 360° - \phi$	$D = \theta - 90°$	$\omega = \arcsin\sqrt{2\frac{1-1/n}{\kappa}}$
Set1	201°	85°	11.22°
Set2	146°	7°	12.05°
Set3	229°	8°	10.20°
Fracture Trace:			
Erlang-2 Distribution	$f(x) = \lambda^2 x e^{-\lambda x}$		
	lambda (λ)		
horizontal	-5.37		
vertical	-3.93		
Fracture Distance:			
Exponential Distribution	$f(x) = \lambda e^{-\lambda x}$		
	lambda (λ)		
	-4.57		
Fracture Density:			
Uniform Distribution	$f(x) = 11.34 \quad m^2/m^3$		

Table 1: Statistics of the fracture geometries observed from the Pliezhausen field block.

Two study cases of SFG (SFG-A and SFG-B) and two study cases of GFG (GFG-A and GFG-B) are considered. The two cases of SFG are set up according to two different assumptions on defining the fracture size. As the fracture size cannot be measured directly from borehole samples or exposed wall surveys, it has to be approximated from the fracture trace observed on the exposed walls by assuming a relation between the fracture size and the observed trace length. In both SFG-A and SFG-B rectangular fractures are assumed. Hence the fracture size can be described by distributions for two of its side-lengths. In SFG-A, the fractures are assumed to have the size directly defined by the fracture-trace distribution shown in Table 1. The length and the width of the horizontal fractures are described by the horizontal trace distribution, whereas the height and the width of the vertical fractures are given by the vertical and the horizontal trace distribution. In SFG-B, the fracture-size distribution is adjusted until the same fracture-trace distribution as for the field block is obtained. The parameter lambda in the erlang-2 distribution describing the horizontal and vertical length

distribution in the SFG-B are 4.28 and 1.70 respectively, instead of 5.37 and 3.93 as in the SFG-A. Reducing the parameter lambda leads to an increase of the fracture size. After the fracture network of the specified fracture geometries (size, orientation and density) has been obtained, the fracture distance is optimized according to the distribution observed from the field block. In the two cases of GFG (GFG-A and GFG-B), an initial configuration of the fracture network is taken from the SFG, where the fracture-distance optimization option is not used, (GFG-A from SFG-A and GFG-B from SFG-B) and then the fracture network is modified by the SA until its spatial parameters similar to those observed from the field outcrop.

Fracture networks are compared in this section by considering two different aspects; one is the structure of the generated fracture networks, and another is the flow and transport behavior of the fracture-matrix systems (FMS). From a stochastic point of view, it is possible to generate multiple realizations of fracture networks such that each realization represents the specified descriptions, however, no single realization can exactly match the real system. The structure of the fracture network and the behavior of the FMS can be quantitatively predicted from the ensemble average which is obtained only when the number of realizations is large enough to assure convergent results. We intend to study but not to predict the characteristics and the behavior of the fractured system, therefore, twenty realizations (five from each study case) are generated. Even though the number of realization seems to be very low, the results of the four cases, which are presented later, show significant differences. For comparing different cases, parameters of each study case are evaluated by averaging over the five exposed walls of each realization and again over all five realizations. The south-west cross-section of one realization from each study case is shown in Figure 10.

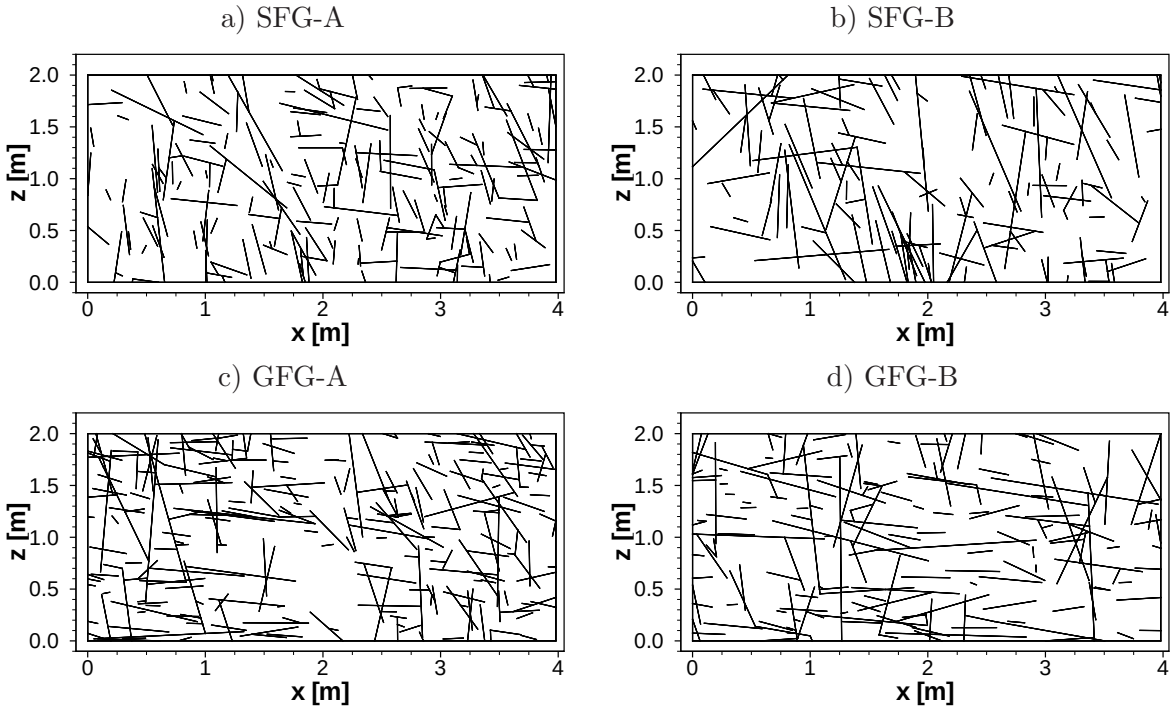

Figure 10: Fracture-trace maps of the south-west exposed wall obtained from the four study cases.

4.1 Structure of a Fracture Network

The fracture networks generated from the four study cases (the SFG-A, the SFG-B, the GFG-A and the GFG-B) are compared with the field block by focusing on the fracture size (fracture trace-length) and the spatial characteristics. The only spatial structure of the fracture network which is considered in the SFG is the fracture distance. On the other hands, the GFG takes into account the spatial characteristics such as standardized experimental variogram, the neighborhoods and the fracture-cell density.

Fracture trace

The average of the cumulated fracture-trace distribution is presented in Figure 11. The result from the SFG-A shows that approximating the fracture size directly from the fracture trace results in a too short trace length distribution, which means the fracture size is underestimated in this case. The SFG-B enlarges the fracture size to fit the fracture-trace distribution, therefore its results show a good agreement with the outcrop. The trace length distribution of the GFG-A changes slightly compared with the SFG-A after optimizing the spatial characteristics. For the GFG-B, the trace-length distribution is smaller than for the SFG-B, which means that optimizing spatial characteristics in this case leads to a reduction of the fracture size.

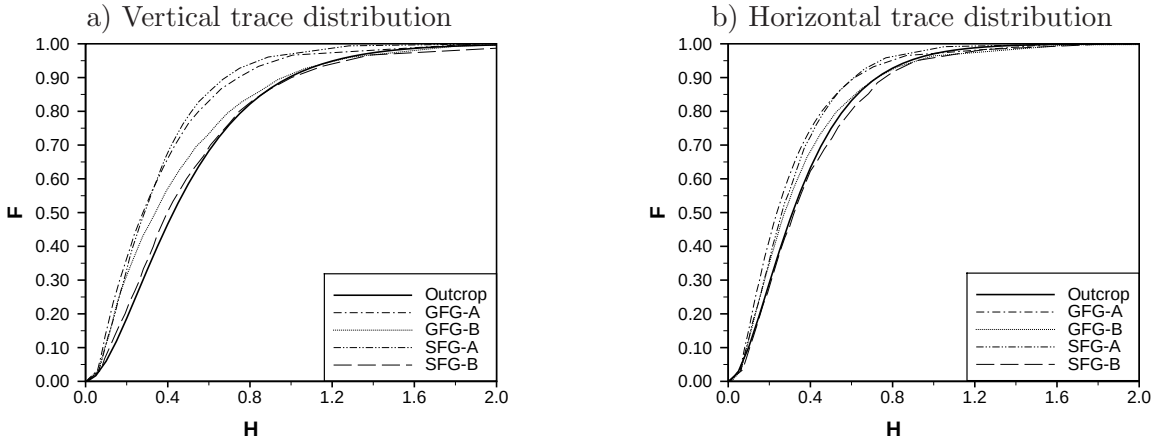

Figure 11: Comparison of the cumulative distribution functions of trace length averaged from the five exposed walls of fracture networks generated from the four study cases.

Fracture distance

Figure 12 shows the cumulated distribution of the fracture distance of the four study cases compared with the field block. The SFG-A and the SFG-B optimize the fracture distance, therefore, they show better agreement with the field value than the GFG-A and the GFG-B. A larger size of fractures in the SFG-B and the GFG-B compared with the SFG-A and the GFG-A means that a less number of fractures are given for the same fracture density, therefore, the distance between two adjacent fractures tends to become longer in the SFG-B and the GFG-B than in the SFG-A and the GFG-A. We do not include the fracture distance as one of the spatial parameter in the geostatistical fracture generator, however, this parameter could be included (if needed).

Standardized experimental variogram

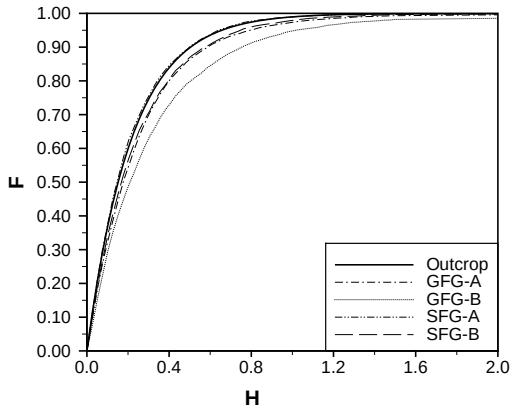

Figure 12: Comparison of the cumulative distribution functions of fracture distance averaged from the five exposed walls of fracture networks generated from the four study cases.

The standardized experimental variogram of the GFG-A and the GFG-B are closer to the outcrop target value than the SFG-A and the SFG-B for the vertical and horizontal fracture-trace directions (Figure 13).

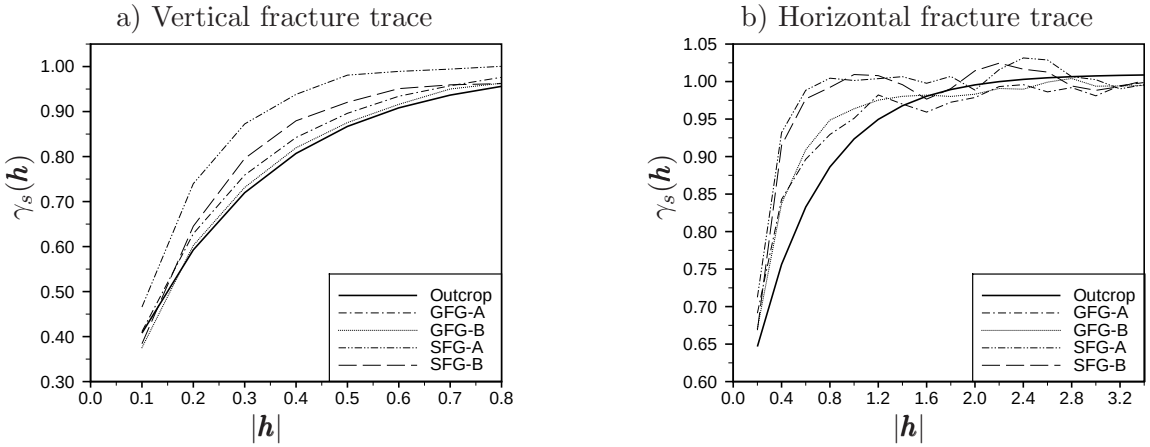

Figure 13: Comparison of the standardized experimental variograms averaged from the five exposed walls of fracture networks generated from the four study cases.

Neighborhoods

The neighborhoods of a fracture and a matrix cell for the vertical fracture trace of the GFG-A and the GFG-B are closer to the field block than the SFG-A and the SFG-B (Figure 14a and 15a). However, the neighborhoods for the horizontal fracture trace of the GFG-A and the GFG-B closely match only in the fracture direction ($k = 2, 3$) but not in the other directions, where the SFG-A and the SFG-B show better results (Figure 14b and 15b). The reason could be that the neighborhoods for the horizontal fracture trace are varied in a range broader than for the vertical fracture trace and tend to be directionally dependent on the south-west walls (see Figure 7b and 8b). Correct representation of a parameter which has this peculiarity might need a more complicated approach. The directional dependence of the neighborhoods is observed

from all realizations generated from the GFG-A and the GFG-B. As shown in Figure 16 and 17, the N_f and the N_m from the field block are close to the values from the north, the east and the west exposed walls but not to the values from the south-east and south-west exposed walls.

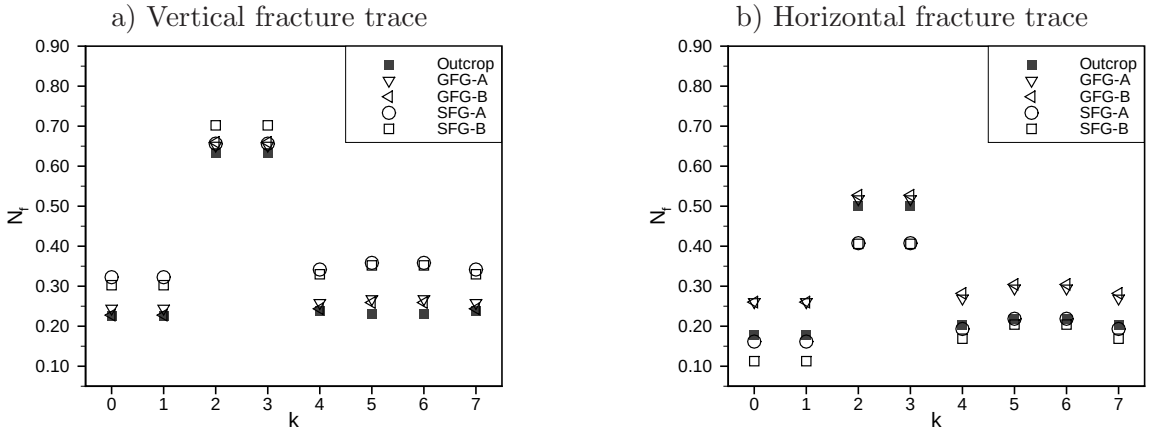

Figure 14: Comparison of the fracture neighborhood averaged from the five exposed walls of fracture networks generated from the four study cases.

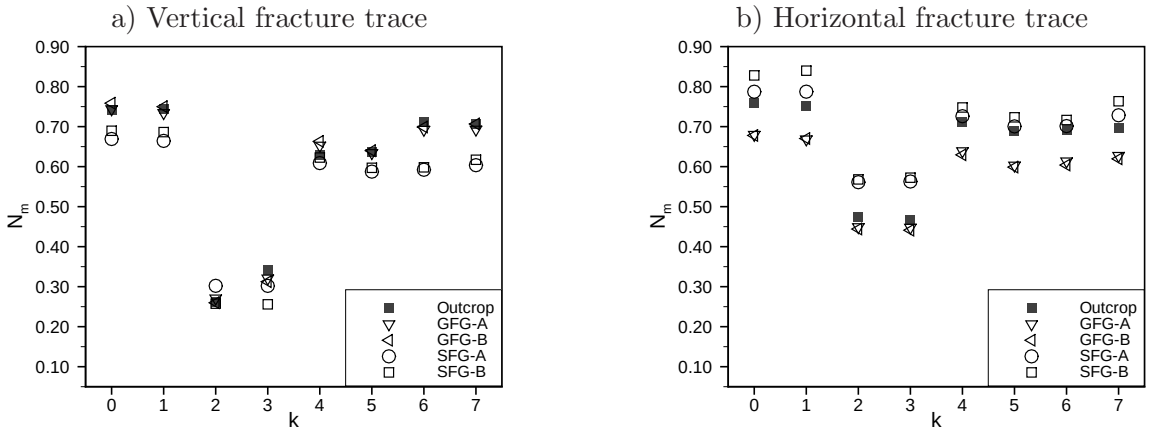

Figure 15: Comparison of the matrix neighborhood averaged from the five exposed walls of fracture networks generated from the four study cases.

Fracture-cell density

The fracture-cell density H evaluated from all cases is shown in Figure 18. The greater number of vertical fractures on the top according to the field outcrop, is only observed from the GFG-A and the GFG-B. The SFG-A and the SFG-B show relatively constant H due to equally distributed fracture cells.

Even though the geostatistical approach (the GFG-A and the GFG-B) does not consider the cumulative distribution of the fracture distance, it still reflects the cumulative distance fairly well. On the other hand, the statistical approach can adequately reproduce the neighborhoods, but not the standardized variogram and the fracture-cell density.

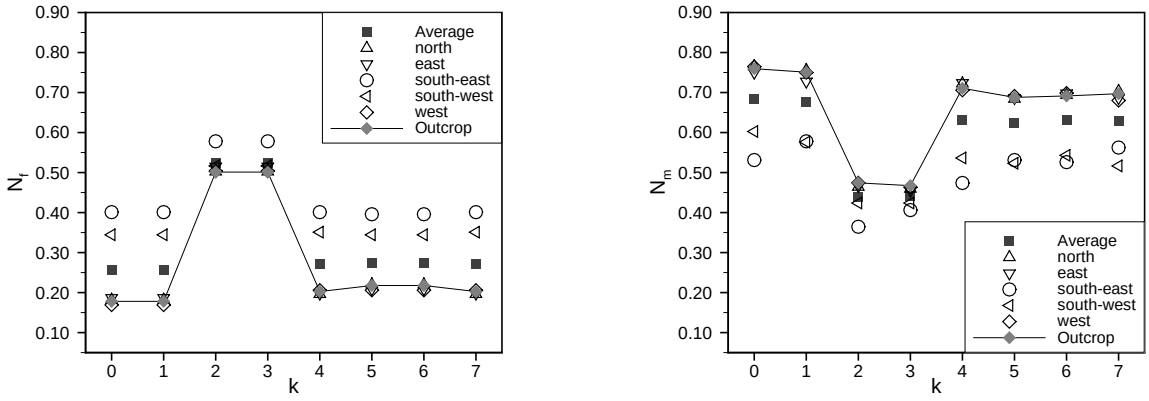

Figure 16: Neighborhoods of one realization of the GFG-A from vertical-scanline indicator fields of the five exposed walls, scanline segment length $l = 0.10\,\mathrm{m}$ and scanline distance $d = 0.20\,\mathrm{m}$.

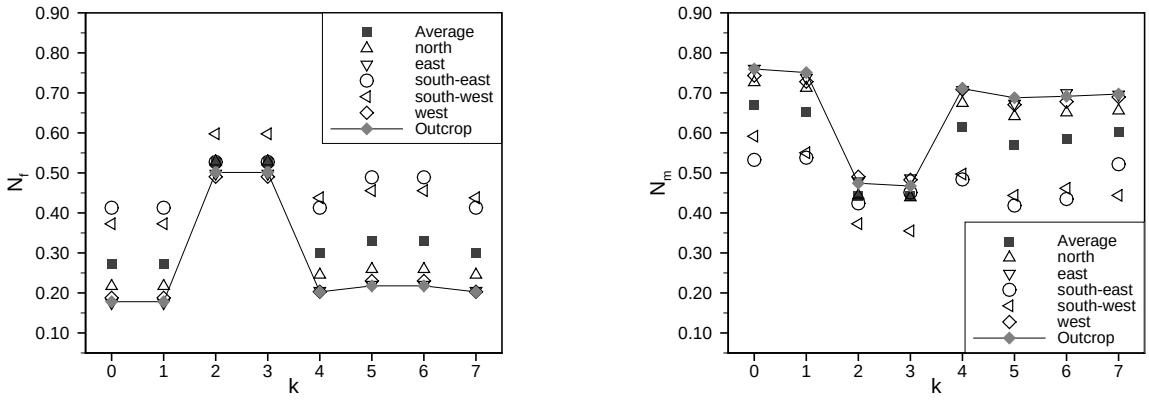

Figure 17: Neighborhoods of one realization of the GFG-B from vertical-scanline indicator fields of the five exposed walls, scanline segment length $l = 0.10\,\mathrm{m}$ and scanline distance $d = 0.20\,\mathrm{m}$.

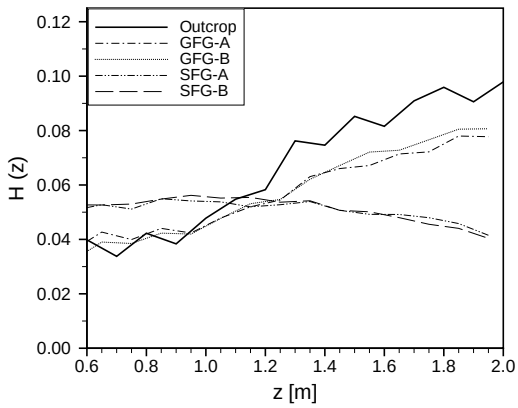

Figure 18: Comparison of the fracture-cell density averaged from the five exposed walls of fracture networks generated from the four study cases for the vertical fracture trace.

4.2 Flow and Transport in a Fracture-matrix System

A comparative study of flow and transport behavior is carried out using the numerical model MUFTE-UG (MUltiphase Flow, Transport and Energy Model - Unstructured Grids) ([15] and [6]).

4.2.1 Formulation of Flow and Transport Equation

For simplicity, steady-state flow of an incompressible single phase in a nondeformable matrix is considered, and source/sink terms are neglected. The continuity equation based on mass conservation can be described as:

$$\nabla \cdot \boldsymbol{q} = 0 \; . \tag{8}$$

Here the velocity $\boldsymbol{q}$ is defined by Darcy's law as a function of the pressure p and the permeability tensor $\boldsymbol{K}$:

$$\boldsymbol{q} = -\frac{\boldsymbol{K}}{\mu}(\nabla p - \rho \boldsymbol{g}) \; , \tag{9}$$

where μ is the fluid viscosity, ρ is the fluid density, and $\boldsymbol{g}$ is the gravitational vector with absolute value equal to the gravitational constant g. Neglecting the gravitational effect in Equation (9) results in

$$\boldsymbol{q} = -\frac{\boldsymbol{K}}{\mu}\nabla p. \tag{10}$$

For fractures a scalar permeability is assumed given by the parallel-plate concept ([33]):

$$K \; = \; \frac{b^2}{12} \; , \tag{11}$$

where b is the fracture aperture.
The governing equation for solute conservative transport process without source/sink terms is given as:

$$\frac{\partial c}{\partial t} + \nabla \cdot (\boldsymbol{v}_s c - \boldsymbol{D}\nabla c) = 0 \; . \tag{12}$$

Here the seepage velocity $\boldsymbol{v}_s$ is a function of the effective porosity ϕ and the Darcy velocity:

$$\boldsymbol{v}_s \; = \; \frac{1}{\phi}\,\boldsymbol{q} \; . \tag{13}$$

The hydrodynamic dispersion $\boldsymbol{D}$ in a two-dimensional case where the transport direction follows the coordinate axis is given as:

$$\boldsymbol{D}_{ij} \; = \; \frac{v_i v_j}{\|\boldsymbol{v}\|}(\alpha_l - \alpha_t) + \delta_{ij}(\alpha_t \|\boldsymbol{v}\| + D_m); \, , \tag{14}$$

where D_m is the molecular diffusion, α_l and α_t are the longitudinal and transversal dispersion lengths, v_x and v_y are the components of seepage velocity in the longitudinal and transversal direction, and the Kronecker delta δ_{ij} is unity for i = j and zero otherwise.

4.2.2 Simulation of Fracture-Network System

The two-dimensional simulations are performed on the south-west cross-sections for the twenty realizations, five from each of the four study cases. These results are compared with a simulation of the scanned south-west wall from the outcrop (Figure 3d). The domain is discretized with a triangular mesh, with lower-dimensional fractures. Then a vertex-centered finite- volume method with upwinding formulation is used to solve Equation 12, see Reichenberger et al. [31] and for details. Boundary conditions are described in Figure 19 and model parameters are shown in Table 2. In this study, a highly advective transport is considered, therefore very low longitudinal and transversal dispersivity are assumed. This advective-dominated transport allows the direct comparison with the results of a streamline method in the accompanying paper ([20]).

		matrix	**fracture**
Permeability, K	$[m^2]$	$1.0 \cdot 10^{-13}$	$8.33 \cdot 10^{-10}$
Eff. porosity, ϕ	[-]	0.13	0.30
Long. dispersivity, α_l	$[m]$	$1.0 \cdot 10^{-9}$	0.0
Trans. dispersivity, α_t	$[m]$	$1.0 \cdot 10^{-9}$	0.0
Diffusion coeff., D_m	$[m^2 s^{-1}]$	$1.0 \cdot 10^{-9}$	$1.0 \cdot 10^{-9}$
Aperture, d	$[m]$	-	$1.0 \cdot 10^{-4}$

Table 2: Flow and transport parameters for all simulations

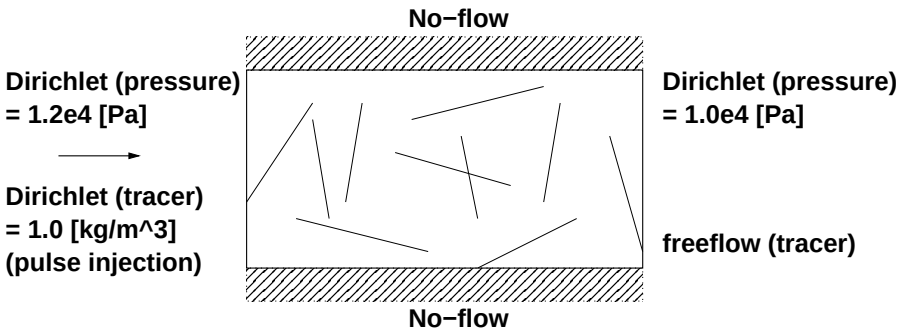

Figure 19: Boundary conditions for flow and transport simulations

The flow and transport behavior of the different case studies are compared with respect to the total outflow Q and the characteristics of the breakthrough curve (BTC) such as a peak mass flux $\dot{m}_p$, a peak arrival time t_p and a mean arrival time $\bar{t}$. The peak mass flux and its arrival time are directly observed from BTCs. The travel time $\bar{t}$ is evaluated from the moment μ_i as:

$$\bar{t} = \frac{\mu_1}{\mu_0} \qquad \text{where} \quad \mu_i = \int_0^\infty t^i c(t) dt \tag{15}$$

Here $c(t)$ is the total mass concentration [kg/s] leaving the domain at time t. The BTCs obtained from transport simulations are shown in Figure 20 and the total discharge Q and the BTC characteristics are summarized in Table 3. The deviation of the simulation results

from the scanned wall is shown in Figure 21, where the standardized value (SV) is defined as

$$SV = \frac{P_r - P_{sw}}{P_{sw}} . \tag{16}$$

Here, P_r is the average of each investigated parameter over the realizations and P_{sw} is the parameter from the scanned south-west wall.

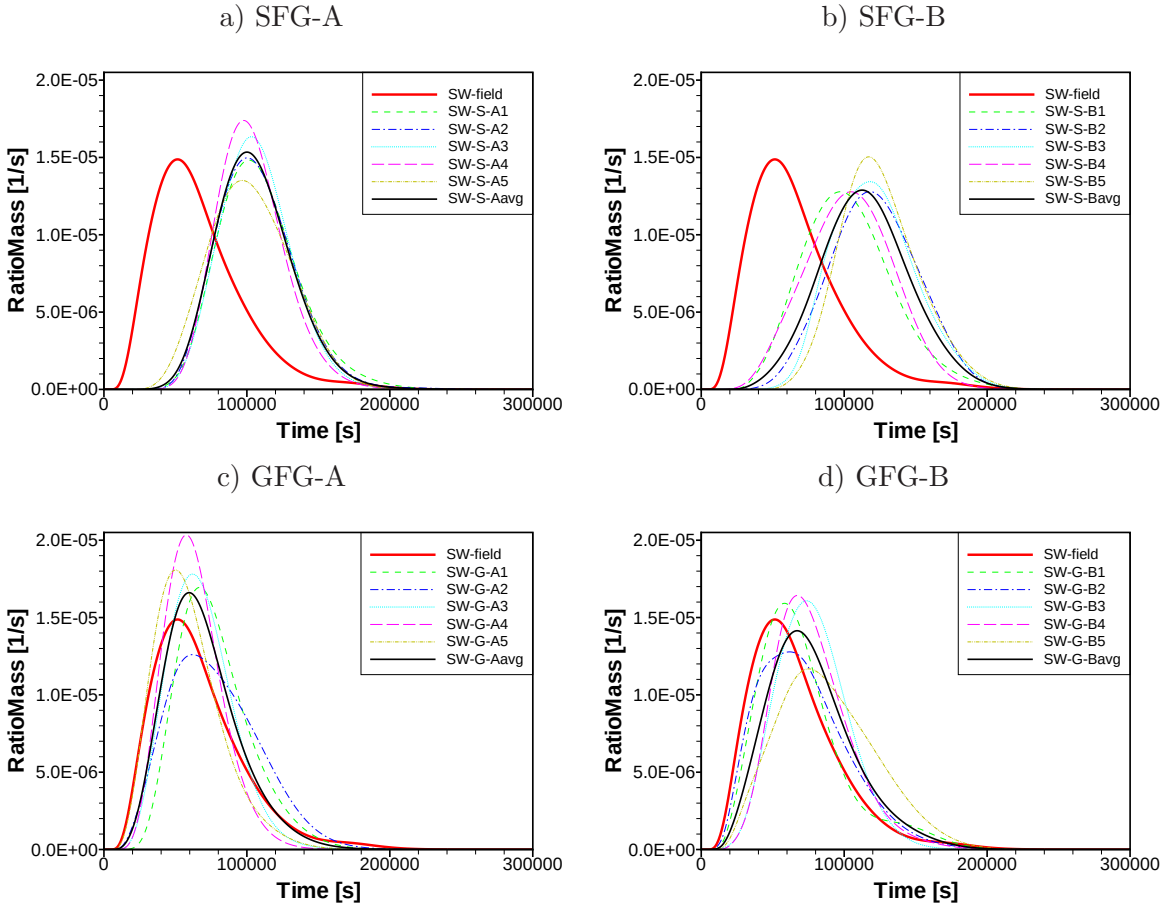

Figure 20: Comparison of breakthrough curves of the south-west walls from different realizations of the four study cases.

The flow and transport behavior of the field outcrop can be, to some extent, represented by GFG-A and GFG-B, however, SFG-A and SFG-B show clearly slower processes (see Figure 20 and Table 3). Compared to the simulated field block, Q, $\bar{t}$ and t_p from GFG-A and GFG-B are closer to the field block than those from SFG-A and SFG-B (see Figure 21). By considering the spatial structures of the fractured system, the connectivity of fractures can be represented. Hence the discharge, the peak arrival time and the mean arrival time can be better approximated. However, connected and preferential flow paths lead to significant variation of the peak mass flux and of the shape of the BTCs. Therefore, the average behavior of the fracture-matrix systems requires a simulation performed on large number of realizations.

The influence of the fracture size observed from the case with and without fracture-trace fitting remains uncertain. The GFG-B shows closer agreement to the outcrop compared with

	Q $[kg\ m^{-3}]$	$\dot{m}_p$ $[kg\ s^{-1}]$	t_p $[s]$	$\bar{t}$ $[s]$
Outcrop	$1.72 \cdot 10^{-5}$	$1.49 \cdot 10^{-5}$	$5.12 \cdot 10^{4}$	$6.64 \cdot 10^{4}$
SFG-A	$1.03 \cdot 10^{-5}$	$1.53 \cdot 10^{-5}$	$1.00 \cdot 10^{5}$	$1.06 \cdot 10^{5}$
SFG-B	$9.36 \cdot 10^{-6}$	$1.29 \cdot 10^{-5}$	$1.13 \cdot 10^{5}$	$1.15 \cdot 10^{5}$
GFG-A	$1.73 \cdot 10^{-5}$	$1.66 \cdot 10^{-5}$	$5.97 \cdot 10^{4}$	$6.90 \cdot 10^{4}$
GFG-B	$1.56 \cdot 10^{-5}$	$1.41 \cdot 10^{-5}$	$6.72 \cdot 10^{4}$	$7.74 \cdot 10^{4}$

Table 3: Results of flow and transport simulations of the south-west wall obtained form the field outcrop and average values from four study cases.

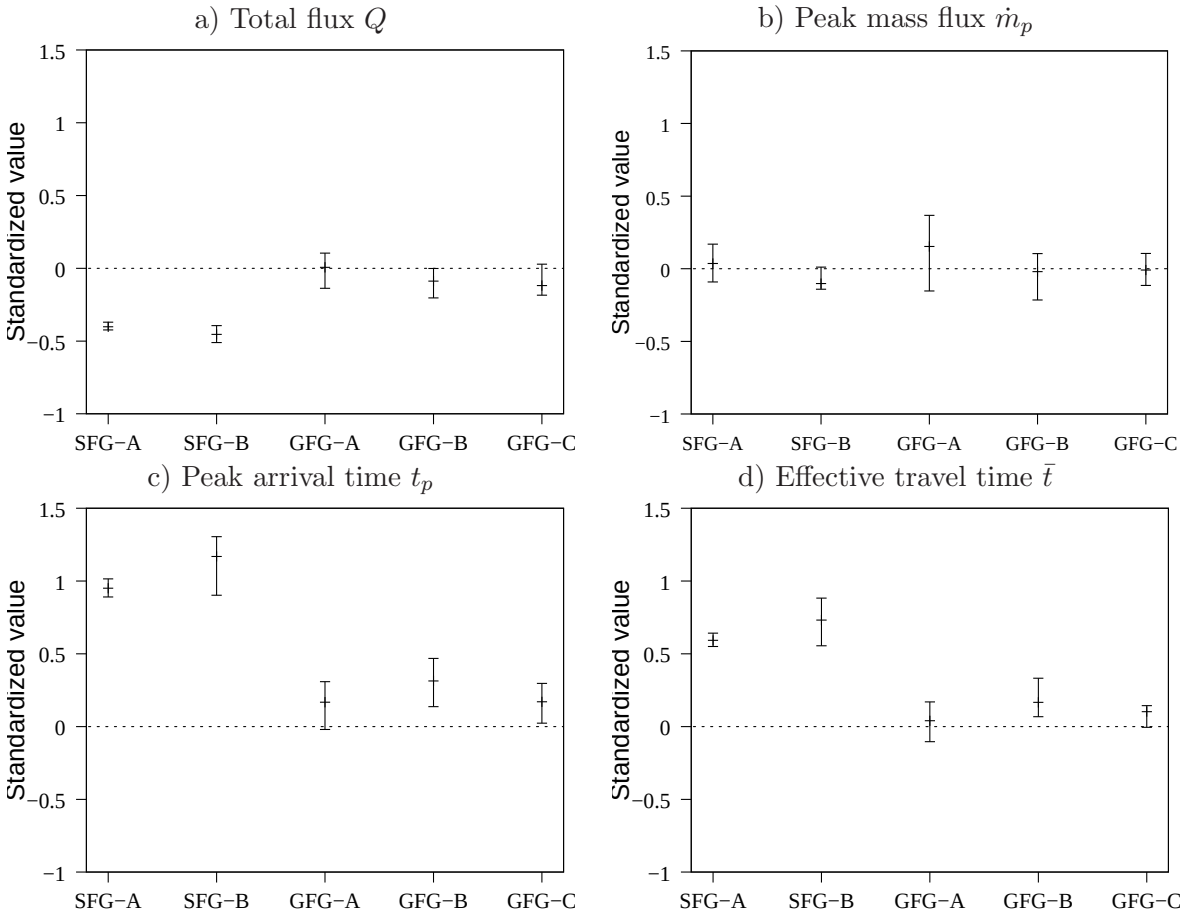

Figure 21: Average and extreme values (min./max.) of flow and transport simulations of the south-west wall of the study cases compared with the results obtained from the field outcrop simulation (dashed line).

the GFG-A for $\dot{m}_p$ but not for Q, t_p and $\bar{t}$. Comparing with the results from the outcrop, the SFG-B seems to be slightly better than the SFG-A for all cases. Investigation on more realizations could be necessary to draw a conclusion about the effect of the fracture size and the average behavior of the systems.
In addition, the influence of numerical diffusion can be noticed by comparing the BTCs of

the scanned south-west wall for different mesh sizes (measured in terms of the average length of the sides of a grid cell): 0.01, 0.02, 0.05, 0.10 and 0.20 m, corresponding to 93547, 23389, 4277, 1177 and 528 grid vertices, respectively. The numerical diffusion in a FMS leads to a surprising result of the BTCs. When the grid sizes become smaller, the variances of the curves become larger and the peak value decreases (see Figure 22). This is due to a physical diffusion caused by the strong heterogeneity between the fractures and the matrix. As shown in Figure 23a and 23b for a fine mesh of 0.02 m, when the injected solute reaches the fractures, it is transported quickly along the fractures and the solute remaining in the matrix requires longer time to transport out of the FMS. On the contrary, for solute transport on a coarse mesh of 0.20 m shown in Figure 23c and 23d, the effect of fast-flowing in the fractures and slow-flowing in the matrix is smeared out over the cross-section perpendicular to the flow direction due to the numerical diffusion. The FMS tends to behave more homogeneous. To guarantee the accuracy of the scheme, a small grid size is necessary, hence, the computational time increases.

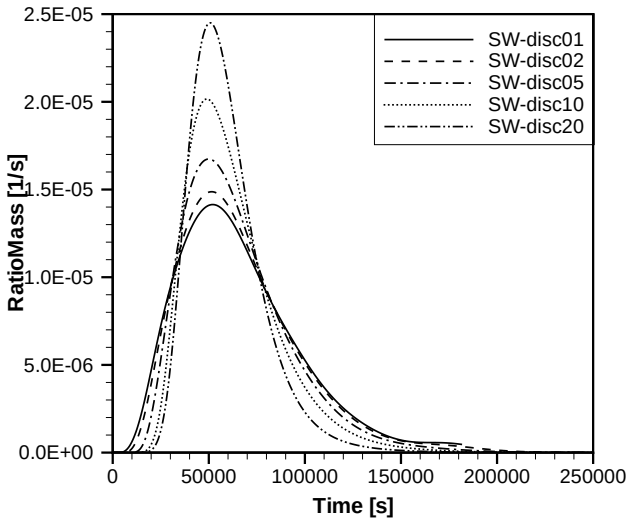

Figure 22: Comparison of breakthrough curves for different mesh sizes: 0.01, 0.02, 0.05, 0.10 and 0.20 m for the south-west exposed wall.

5 Conclusion and Outlook

A geostatistical fracture generator (GFG) which integrates statistical geometries and spatial characteristics has been presented in this work. By applying a modified scanline technique, fracture-trace maps of exposed walls are transformed to indicator fields on which the spatial characteristics are quantified in terms of the standardized variogram, the neighborhoods and the fracture-cell density. Simulated annealing is selected as our methodology for integrating the spatial characteristics in the GFG. We have shown here that fracture networks generated by the GFG not only can reproduce the chosen spatial characteristics, but also, to some extent, can represent the cumulative distribution of the fracture distance observed from the field which is not included in the GFG. The fracture networks created by the statistical fracture

a) Mesh size 0.02 m, t 200 s

b) Mesh size 0.02 m, t 32000 s

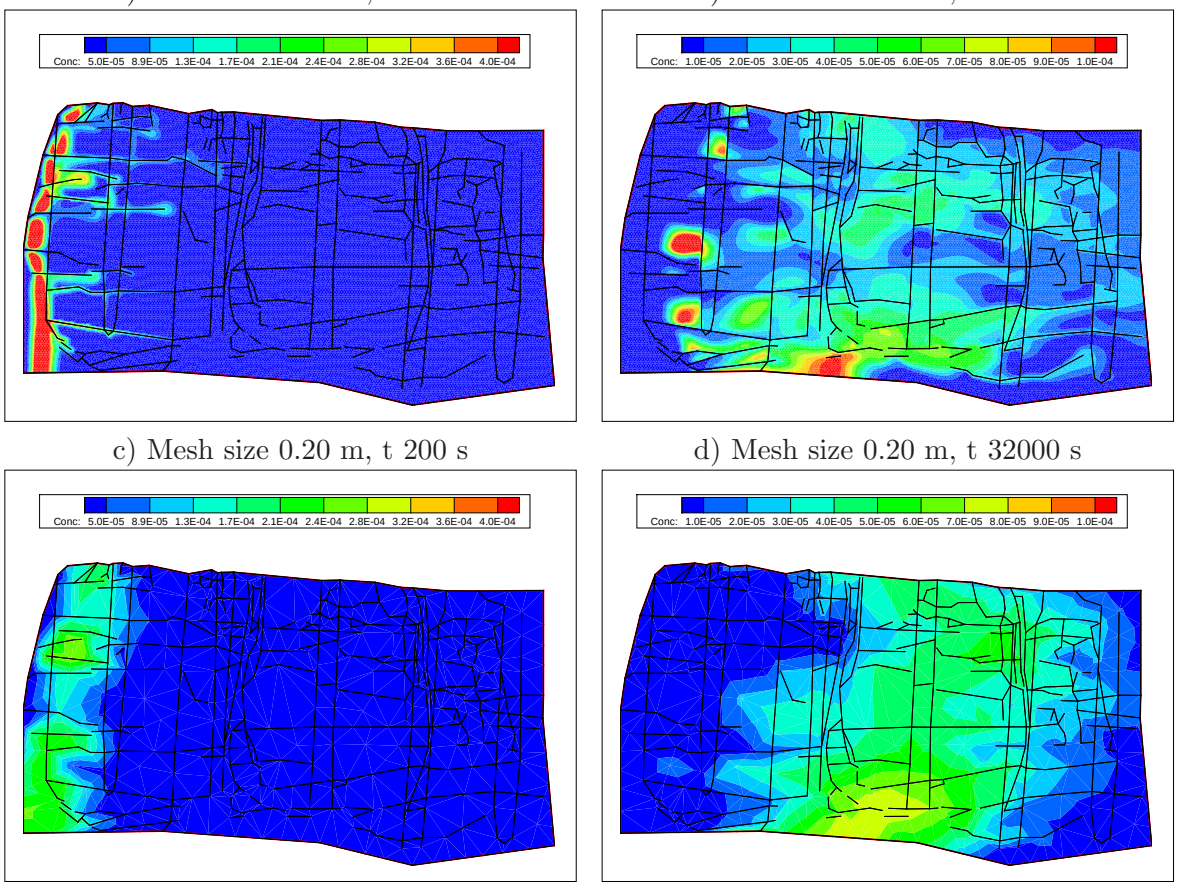

c) Mesh size 0.20 m, t 200 s

d) Mesh size 0.20 m, t 32000 s

Figure 23: Concentration distribution for the south-west wall at time 200 and 32000 s using mesh sizes 0.02 (fine grid) and 0.20 (coarse grid) m.

generator (SFG) show good results for the fracture-distance distribution and reasonably good results for the neighborhoods, however not for the standardized variogram and the fracture-cell density. Further, strong influence of the spatial characteristics was clearly demonstrated in flow and transport simulations. The GFG can better capture the system behavior such as the discharge, the peak arrival time and the mean arrival time than the two study cases from the SFG. Integrating the spatial characteristics and the statistical geometries in the GFG have improved the discrete fracture generation and, therefore, the behavior of the fractured system can be better predicted. Considering only the fracture distance as a spatial structure and the statistical geometries as in the SFG is not sufficient in this case to generate a "representative" fracture network. Additional spatial parameters such as the standardized variogram, the neighborhoods and the fracture-cell density must also be considered.
The flow and transport process in a three-dimensional fracture-matrix system should be further investigated, since the connectivity of fractures in 3D becomes even more complex than in 2D. Considering this effect might lead to an effort on extending the geostatistical fracture generator to take into account additional spatial characteristics.
Due to the strong heterogeneity between fractures and the surrounding matrix and the numerical diffusion, accurate results of flow and transport simulations in a fracture-matrix system can only be obtained on a fine mesh. This means that an approach that performs fast with less numerical diffusion is essential. In an accompanying paper ([20]), we present an application of streamline tracing on a fracture-matrix system. The advantages of the streamline method is that it is extremely fast compared with the standard finite volume scheme (which is used here) and, at the same time, does not suffer from numerical diffusion.

6 Acknowledgments

This work was supported by the International Research Training Group "Non-Linearities and Upscaling in Porous Media (NUPUS)" financed by the German Research Foundation (DFG) and in parts by the Norwegian Research Council, StatoilHydro, and Norske Shell under grant no. 178013/13. The authors would like to thank Wolfgang Nowak for his valuable comments on the manuscript.

References

[1] Aarts, E., and J. Korst, *Simulated annealing and Boltzmann machines*, John Wiley & Sons, 1989.

[2] Alexander, J., *A discussion on the use of analogues for reservoir geology*, In ASHTON, M. (Ed.), *Advances in Reservoir Geology*, Geological Society, Special Publications, n. 69, 175-194, 1992.

[3] Assteerawatt, A., *Flow and Transport Modelling of Fractured Aquifers based on a Geostatistical Approach*, (http://elib.uni-stuttgart.de/opus/volltexte/2008/3639/), PhD Thesis, Universität Stuttgart, Institute of Hydraulic Engineering, 2008.

[4] Soares, A., A. Brusco, and C. Guimaraes, Simulation of Naturally Fractured Fields, *Geostatistics Wollongong '96 (Quantitative Geology and Geostatistics)*, Kluwer Academic Publishers, 1997.

[5] Bárdossy, A., Generating precipitation time series using Simulated Annealing. *Water Resour. Res., 34(7)*, 1737 - 1744, 1998.

[6] Bastian, P., K. Birken, S. Lang, K. Eckstein, N. Neuss, H. Rentz-Reichert, and C. Wieners, UG - A Flexible Software Toolbox for solving partial differential equations, *Computing and Visualization in Science*, 1997.

[7] Bear, J., *Dynamics of Fluids in Porous Media*, Academic Press, 1972.

[8] Berkowitz, B., Characterizing flow and transport in fractured geological media: A review, *Adv. Water Resour., 25*, 861-884, 2002.

[9] Billaux, D., J. Chiles, K. Hestira, and J. Longa, Three-dimensional statistical modelling of a fractured rock mass–an example from the Fanay-Augères mine, *Int. J. Rock Mech. Min. Sci. Geomech. Abstr. 26(3,4)*, 281-299, 1989.

[10] Bodvarsson, G., and Y. Tsang, Special issue: Yucca mountain project, *J. Contam. Hydrol. , 38*, 1-425, 1999.

[11] Bodvarsson, G., C. Ho, and B. Robinson, Special issue: Yucca mountain project, *J. Contam. Hydrol. , 62-63*, 1-750, 2003.

[12] Cacas, M., E. Ledoux, G. de Marsily, A. Barbreau, P. Calmels, B. Gaillard, and R. Margritta, Modeling Fracture Flow With a Stochastic Discrete Fracture Network: Calibration and Validation 2. The Transport Model, *Water Resour. Res., 26(3)*, 491-500, 1990.

[13] Cacas, M., E. Ledoux, G. de Marsily, B. Tillie, A. Barbreau, E. Durand, B. Feuga, and P. Peaudecerf, Modeling Fracture Flow With a Stochastic Discrete Fracture Network. Calibration and Validation 1. The Flow Model, *Water Resour. Res., 26(3)*, 479-489, 1990.

[14] Chilés, J., and P. Delfiner, Geostatistics: Modeling Spatial Uncertainty, *Wiley series in probability and mathematical statistics*, John Wiley & Sons, Inc., 1999.

[15] Helmig, R., H. Class, R. Huber, H. Sheta, R. Ewing, R. Hinkelmann, H. Jakobs, and P. Bastian, Architecture of the Modular Program System MUFTE-UG for Simulating Multiphase Flow and Transport Processes in Heterogeneous Porous Media, *Mathematische Geologie, 2*, 123-131, 1998.

[16] Day-Lewis, F., P. Hsieh, and S. Gorelick, Identifying fracture-zone geometry using simulated annealing and hydraulic-connection data, *Water Resour. Res., 36(7)*, 1707-1721, 2000.

[17] Deutsch, C., and P. Cockerham, Practical considerations in the application of simulated annealing to stochastic simulation, *Math. Geol., 26(1)*, 67-82, 1994.

[18] Dietrich, P., R. Helmig, M. Sauter, H. Hötzl, J.Köngeter, and G. Teutsch, *Flow and Transport in Fractured Porous Media*, Springer-Verlag, 2005.

[19] Dverstorp, B., and J. Andersson, Application of the Discrete Fracture Network Concept with Field Data: Possibilities of Model Calibration and Validation, *Water Resour. Res., 25(3)*, 540-550, 1989.

[20] Hægland, H., A. Assteerawatt, R. Helmig, and H.K. Dahle, Simulation of flow and transport in discrete fracture-matrix system: II. Efficient and accurate streamline approach, *Water Resour. Res.*, submitted, 2008.

[21] Kirkpatrick, S., C. D. Gelatt Jr., and M. Vecchi, Optimization by Simulated Annealing, *Science, 220*, 671-680, 1983.

[22] La Pointe, P., and J. Hudson, Characterization and interpretation of rock mass joint patterns, *Special paper 199, Geological Society of America*, 1985.

[23] Long, J., *Investigation of equivalent porous medium permeability in networks of discontinuous fractures*, PhD Thesis, Berkley, 1983.

[24] Long, J., and D. Billaux, From Field Data to Fracture Network Modeling: An Example Incorporating Spatial Structure, *Water Resour. Res., 23(7)*, 1201-1216, 1987.

[25] Long, J., J. Remer, C. Wilson, and P. Witherspoon, Porous Media Equivalents for Networks of Discontinuous Fractures, *Water Resour. Res., 18(3)*, 645-658, 1982.

[26] Mauldon, A., K. Karasaki, S. Martel, J. Long, M. Landsfeld, A. Mensch, and S. Vomvoris, An inverse technique for developing models for fluid flow in fracture systems using simulated annealing, *Water Resour. Res., 29(11)* 3775-3789, 1993.

[27] Metropolis, N., A. Rosenbluth, M. Rosenbluth, A. Teller, and E. Teller, Equations of state calculations by fast computing machines, *J. Chem. Phys., 21*, 1087-1092, 1953.

[28] National Research Council, *Rock Fractures and Fluid Flow*, National Academic Press, 1996.

[29] Pannatier, Y., *VARIOWIN: Software for spatial data analysis in 2D*, Springer-Verlag, 1996.

[30] Poteri, A., D. Billaux, B. Dershowitz, J.J. Gomez Hernandez, V. Cvetkovic, A. Hautojärvi, D. Holton, A. Medina, and A. Winberg, Final report of the TRUE Block Scale project. 3. Modelling of flow and transport, *Technical report, Swedish Nuclear Fuel and Waste Management Company (SKB)*, TR-02-15, 2002.

[31] Reichenberger, V., H. Jakobs, P. Bastian, and R. Helmig, A mixed-dimensional finite volume method for two-phase flow in fractured porous media, *Adv. Water Resour., 29(7)*, 1020-1036, 2006.

[32] Silberhorn-Hemminger, A., *Modellierung von Kluftaquifersystemen: Geostatistische Analyse und deterministisch – stochastische Kluftgenerierung*, PhD Thesis, Mitteilungen H. 114 , Institut für Wasserbau, Universität Stuttgart, 2002.

[33] Snow, D.T., Anisotropic permeability of fractured media, *Water Resour. Res., 5(6)*, 1273-1289, 1969.

[34] Tran, N., Simulated annealing technique in discrete fracture network inversion: optimizing the optimization, *Comput. Geosci., 11(3)*, 249-260, 2007.

[35] Tran, N., Z. Chen, and S. Rahman. Integrated conditional global optimisation for discrete fracture network modelling, *Comput. Geosci., 32(1)*, 17-27, 2006.

[36] Wollrath J., Ein Strömungs- und Transportmodell für klüftiges Gestein und Untersuchungen zu homogenen Ersatzsystemen, *Technical Report 28*, Institut für Strömungsmechanik und Elektronisches Rechnen im Bauwesen, Universität Hannover, 1990.